

# Progress in 3D/4D Material Science toward Ferrous Materials

## 3D/4D マテリアルサイエンスの鉄鋼材料への展開

Hiroyuki Toda

Professor, Department of Mechanical Engineering, Toyohashi University of Technology,  
Toyohashi, Aichi 441-8580, Japan

### Introduction

Over the past decade, attempts have been made to apply synchrotron X-ray microtomography (XMT) to ferrous materials, as the importance of 3D observation has been recognized. XMT performed on light materials has generally enabled the reconstruction of volumes with maximum spatial resolution close to the physical limit of the projection-type set-up (approximately 1  $\mu\text{m}$ )<sup>1,2)</sup>. However, in the case of ferrous materials, difficulties arise with respect to X-ray transmission. Since photoelectric absorption is dramatically enhanced with increasing atomic number, high energy X-rays are needed to realize X-ray imaging for ferrous materials. This can lead to spatial resolution degradation, in addition to image quality degradation due to poor photon statistics. For example, Everette et al. and Lame et al. have utilized white X-rays to observe steel at a spatial resolution of 3 and 2.7  $\mu\text{m}$  (not on ferrous materials, but on Cu), respectively<sup>3,4)</sup>. Cheong et al. (90 keV X-ray was used for field of view of 4.34 mm) and Shobu et al. (66.4 keV X-ray was used for field of view of 5.97 mm) used monochromatic X-rays from undulators<sup>5,6)</sup>; and although no measurement or description of spatial resolution is presented in their papers, spatial resolutions of 19 and 35  $\mu\text{m}$ , respectively, are expected at best, according to the descriptions of sample size and the number of projections. This technological limitation prevents us from utilizing advanced applications of XMT, such as measurements of 3D/4D crack-tip displacement/strain fields<sup>7)</sup>, local crack driving forces<sup>8)</sup>, and the spatial distribution of chemical concentrations<sup>9)</sup>, which have been developed mainly using light materials. It would therefore be of significant value to attain the best achievable spatial resolution level for ferrous materials.

The past decade has also witnessed an explosive growth in the XMT technique using large synchrotron sources (e.g., SPring-8, ESRF) for studying the fracture and fatigue behaviour of engineering materials<sup>10)</sup>. The development of techniques such as 3-D strain mapping<sup>11)</sup>, K-edge subtraction<sup>12)</sup> and local crack driving force mapping<sup>8)</sup> from the reconstructed images obtained from the in-situ XMT experiments in synchrotron radiation facilities have provided new insights on the failure of alloys, foams and composites<sup>8,9,13-16)</sup>. The availability of 3-D images containing internal microstructural information provides the unique opportunity for investigating the development of cavities during creep of material. Recent investigation on the development of creep damage (voids and cracks) in a Fe-Ni-Cr fully austenitic steel using synchrotron beam line at Spring-8 provided quantitative characterization of the void content in the as-cast and ex-service variants of the material<sup>5)</sup>.

In the present study, an XMT study was performed at a synchrotron radiation facility to examine the effects of various experimental parameters on spatial resolution. Fatigue crack opening behaviors were then evaluated, and advanced analysis performed, by applying the optimal experimental conditions obtained. Study on the evolution of voids due to creep deformation in 9-12%Cr tempered martensitic steels was also carried out with the subsequent quantitative analysis concerning the creep stress and holding time dependent behaviors.

## 2. Experimental procedure

### 2.1 XMT setup

XMT was performed at the undulator beamline BL20XU of the SPring-8. A monochromatic X-ray beam, produced by a liquid nitrogen-cooled Si (511)-(333) double crystal monochromator, was used. The image detector consisted of a cooled 4000 (H)  $\times$  2624 (V) element CCD camera (pixel size of the camera: 5.9  $\mu\text{m}$  square) in 2 $\times$ 2 binning mode, a scintillator ( $\text{Lu}_2\text{SiO}_5\text{:Ce}$ ), and an optical microscope (OM) objective lens ( $\times 20$ ). Thickness of the LSO scintillator was 10 and 26  $\mu\text{m}$  for 40 and 55/70 keV, respectively. In total, 1500 radiographs, scanning 180 degrees, were obtained in 0.12 degree increments. As mentioned above, the theoretical limit of the projection-type XMT is approximately 1  $\mu\text{m}$ , which is determined primarily by inevitable image blurring caused by Fresnel diffraction, the diffraction limit of visible light, and the spatial resolution of a scintillator<sup>17</sup>). Isotropic voxels (a volume element in 3D space) with 0.5  $\mu\text{m}$  edges, that were requisite to achieve the 1  $\mu\text{m}$  spatial resolution, were achieved in the reconstructed slices. In order to realize high-resolution imaging for ferrous materials, high photon energies of 40~70 keV were used in this study.

### 2.2 Spatial resolution evaluation

First purpose of this study was to optimize the spatial resolution of the XMT setup at high X-ray energies, by varying experimental parameters. Test patterns were designed to test spatial resolution. The test patterns consisted of pairs of lateral and vertical gratings with increasing line pitch between 1.36~2.65  $\mu\text{m}$  and 1.32~2.47  $\mu\text{m}$ , respectively, as shown in Fig. 1. The test patterns were machined on a stainless steel wire of about 497  $\mu\text{m}$  in diameter using the focused ion beam milling technique. The modulation transfer function (MTF) derived from an edge response function (ERF) at the outer contour of the wire (i.e., the steel/air interface) was also measured, to determine the spatial resolution at 5 % contrast ratio. This measurement corresponds to the lateral direction, which is the circumferential direction with respect to the stainless steel wire axis. The test-pattern wire was scanned at 40, 55 and 70 keV, with varying sample/detector distance. The results of the interface-based MTF calculations and the subjective inspection of the test patterns suggested fundamentally reasonable agreement.



Fig. 1 A resolution test object that has been prepared on a stainless-steel wire of about 497  $\mu\text{m}$  in diameter using the focused ion beam technique. The three arrows indicate three directions along which spatial resolution was measured.

### 2.3 Fatigue crack observation

Material used in this section was S15C carbon steel, which exhibits a ferritic-martensitic structure with comparatively large areas of martensite due to a special heat treatment. Its chemical composition was 0.15C-0.15Si-0.41Mn-0.014P-0.008S and balance Fe in mass %. A specimen of 22 mm  $L \times$  0.48 mm  $W \times$  0.48 mm  $B$  with a corner fatigue crack was prepared in the form of an I-shaped specimen. The values of  $W$  and  $B$  are within a 0.6 mm long gauge length. The fatigue pre-crack was introduced with a load ratio  $P_{\min}/P_{\max}$  of 0.1 and maximum stress of 350 MPa.

Photon energy of 40 keV and sample/detector distance of 110 mm were adopted. The entire cross-section of the specimen and a region of about 650  $\mu\text{m}$ -high around the crack were captured on the CCD camera. An in-situ loading rig, which had been specially designed for the in-situ XMT observation, allowed specimens to be scanned under cyclic loading with a load resolution of 0.1 N and a displacement stability of about 0.1~0.2  $\mu\text{m}$ . A first scan of the tomography was performed without loading (2.4 N). Subsequent scans were performed at 6.7, 13.4, 20.2, 26.9, 33.6 and 60.0 N, after the relaxation behavior of the material was stabilized. Image slices were reconstructed from the series of projections, based on a conventional filtered back-projection algorithm<sup>18)</sup>. The gray value in each dataset was calibrated so that the linear absorption coefficient of 3~50  $\text{cm}^{-1}$  fell within an 8-bit gray scale range between 0 and 255.

To calculate the gravity center of each particle and pore with sub-voxel accuracy, pentagonal faceted iso-intensity surfaces were computed from the volumetric data set using the conventional marching cubes algorithm<sup>19)</sup>. To suppress inaccuracies originating from image noise, only particles over 27 voxels in volume were counted for particle tracking. The particles were tracked throughout the tensile loading by employing a matching probability parameter (MPP) method, called the modified spring model which we had previously developed<sup>11,20)</sup>. The optimal values of coefficients  $\alpha$ ,  $\beta$  and  $\gamma$  in the MPP were identified as 0.8, 0.1, and 0.1, respectively. Tetrahedra with all the particles and pores as vertices in the 3D image were created by the Delaunay tessellation technique to calculate internal strain in 3D in high density<sup>20,21)</sup>. All the strain components were calculated from the displacement of the vertices of the tetrahedrons, assuming that the displacement in a given tetrahedron is a linear function. Crack-tip opening displacement (CTOD) was also measured on each slice.

## 2.4 Void observation in creep samples

Typical 9-12% Cr heat resistant steel with nominal chemical compositions of 12Cr-2W-1Cu-0.6Mn-0.4Mo-0.2V-0.1C-0.1Si-bal.Fe (in mass%) was selected for this investigation. The samples have been crept after quenched and tempering treatment involving austenitizing at 1373 K for 8 h, followed by aging at 1003 K for 36 h. The stress rupture tests were carried out with periodic interruptions to measure their elongations until failure at 873 K. Applied nominal stresses were ranged within 120~180 MPa. Coupon samples with a square cross-section of about 300 $\times$ 300  $\mu\text{m}^2$  were extracted from the each crept specimen to investigate their voids evolution using synchrotron XMT in Spring-8. The undulator beamline BL20XU was tuned to produce a beam of energy 40 keV and a detector distance was 110 mm from sample. To evaluate the creep cavities, a local threshold of grey value was assigned and only those greater than 3 $\times$ 3 $\times$ 3 connected voxels were selected. A marching cubes algorithm was utilized to determine the number, volume, surface area and gravity center of voids in the reconstructed region of interest.

## 3. Results and discussion

### 3.1 Spatial resolution

Fig. 2 shows the virtual cross-sections captured at a sample/detector distance of 110 mm. Even the narrowest grating was resolved with each of the three X-ray energies used. The variations in lateral (radial with respect to the stainless-steel wire axis) and vertical resolution with sample/detector distance are shown in Figs. 3(a) and 3(b), respectively. It can be confirmed that the vertical resolution exceeds the lateral resolution, at least at 55 and 70 keV. The lateral resolution results further reveal that spatial resolution worsens when the sample is closer to the detector. This is probably due to the effects of X-ray scattering. It is well known that at a relatively low X-ray energy range (~20 keV) the X-ray scattering distribution is approximately isotropic, while increasing the X-ray energy causes a preferential forward scattering<sup>22)</sup>. The X-

ray photons that are forward directed are more apt to be detected by the image detector when the sample/detector distance is small, thereby reducing spatial resolution.

Fig. 3(c) shows the variations in lateral (circumferential with respect to the stainless-steel wire axis) direction with respect to the spatial resolution that were obtained by means of MTF. Although the lateral resolution appears to differ between Figs. 3(b) and 3(c), it should be noted that the measuring directions differ between Figs. 3(b) (circumferential direction) and (c) (radial direction) with respect to the stainless-steel wire axis. Comparisons of all the resolution data shown in Fig. 3 indicate that the spatial resolution is unexpectedly highest in all three directions when the X-ray energy is 70 keV. This may be associated with the characteristics of the Lutetium-based scintillator employed. The size of the volume in the scintillator in which X-rays are absorbed and scintillation photons are produced is generally dependent on the X-ray energy. If this volume is less than the diffraction-limited resolution of the optical system used, the spatial resolution of the system is not limited by the X-ray absorption process. It is however reasonable to assume that the absorption mean free path of X-ray radiation depends on photon energy at high X-ray energies. Hence, it may be assumed that the lower the photon energy is, the better the resolution achieved in the image. This is because the spreading of the visible photons produced in the scintillator acts to blur the image. It is however interesting to note that Lu has K absorption edge at 63.314 keV and this inevitably causes the smallest absorption mean free path at 70 keV among the three X-ray energies employed, thereby resulting in beneficial effects on spatial resolution.

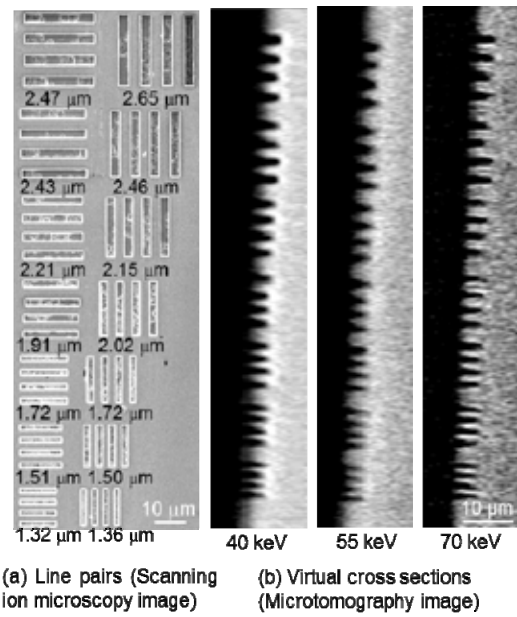


Fig. 2 Virtual cross-sections captured at sample/detector distance of 110 mm, showing how the lateral gratings for vertical resolution evaluation can be resolved at the three X-ray energies. Note that even the narrowest grating was resolved with the three X-ray energies used.

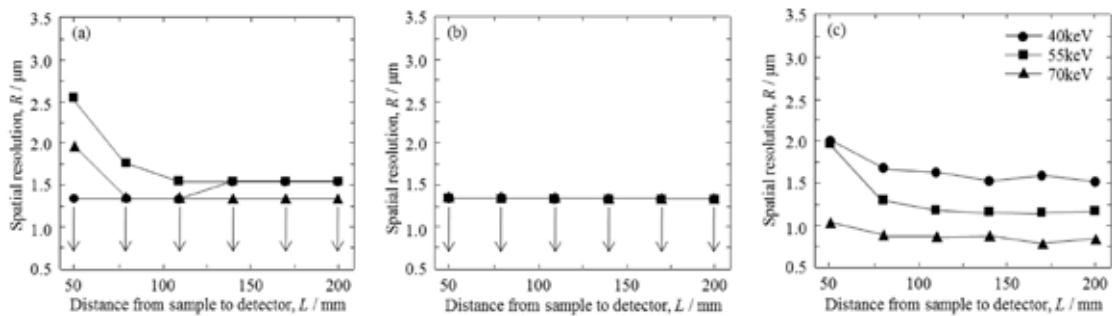


Fig. 3 Variation in spatial resolution in (a) lateral (circumferential), (b) vertical and (c) lateral (radial) directions with respect to the rotation axis; (a) and (b) were obtained through subjective evaluation of the resolution test object, while (c) was determined with MTFs derived from ERFs at the outer contour of the wire. Spatial resolution was defined at modulation transfer function of 5 %. Original line spread functions were fitted with a sigmoid function.

Fig. 4 shows edge response functions revealing the degree of blurring at the sharp air/steel interface. Obvious overshoot and undershoot may be observed in the profiles. Since these are caused by X-ray refraction at the interface, the extent of the overshoot and undershoot increases with the increase in distance. And, it is qualitatively evident that spatial resolution is not significantly different among the three conditions. A total of eight measurements were averaged for each ERF. A line spread function (LSF) was obtained by taking the first derivative from each ERF that had been fitted with a sigmoid function. MTF was then derived by applying discrete Fourier transform to the LSF.

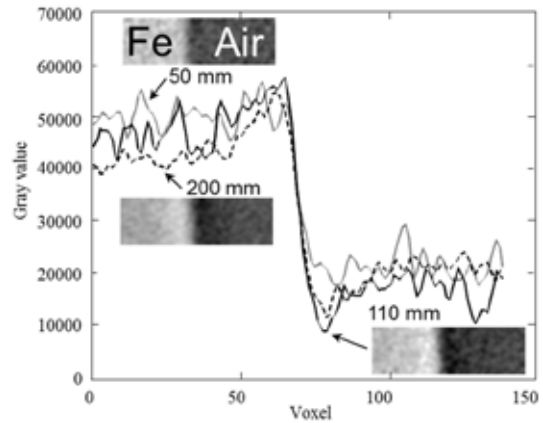


Fig. 4 ERFs (which indicate how original images are spread out) at X-ray energy of 55 keV according to various sample/detector distances, used to calculate MTFs of 3D images.

### 3.2 Fatigue crack visualization

Owing to the superior spatial resolution level attained, both cracks and some microstructural features of the underlying steel could be clearly visualized. In total, 1,249 dispersion particles and 1,687 micropores were confirmed in the entire rendered volume. The particle volume fraction was 0.04 % and the mean equivalent diameter was 4.3  $\mu\text{m}$ , while those for the micropores were 0.11 % and 5.4  $\mu\text{m}$ , respectively, as shown in Fig. 5. The particles and pores are limited to those larger than 27 voxels in volume. It may be inferred that the number of visible microstructural features is somehow enough to derive various internal mechanical quantities such as stress/strain and local crack driving forces. In Fig. 5, only crack images were extracted from the tomographic volume captured at 2.4 N, and the underlying metal and other microstructural features are not displayed. They are shown as 3D perspective images viewed in the mode I loading direction in Fig. 5(a) and the crack mouth direction in Fig. 5(c). Fig. 5(b) is an OM image that corresponds to Fig. 5(c). Fig. 5(a) reveals the distribution of some fatigue crack closure patches (indicated by black arrows), that don't completely disappear even at relatively high load levels. It has been well documented in the literature that such scattered closure patches contribute effectively to fatigue crack growth resistance<sup>23,24</sup>.

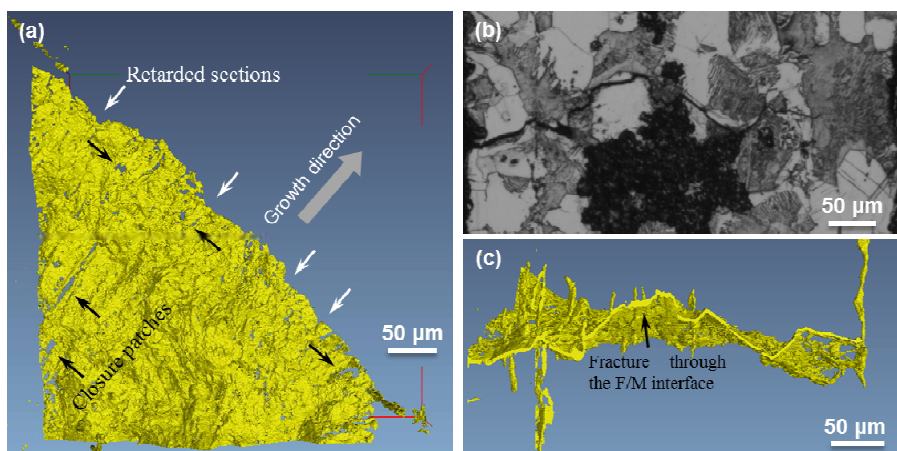


Fig. 5 3D perspective views of a fatigue crack. Only cracks have been extracted from the tomographic volume as shown in (a) and (c); (b) is an OM image that corresponds to (c).

Crack extension varied to some extent along the crack front line. A few retarded sections of the crack front are seen periodically, as indicated by white arrows in Fig. 5(a), together with some fracture surface roughness. Other noteworthy features are the significant crack deflection and tilting caused by the occurrence of modes II and III driving forces, respectively, which can be more obviously identified in Fig. 5(c). In fact, the underlying phases have been identified, as shown in Fig. 5(b), as the ductile ferrite phase and the less ductile martensite phase<sup>25)</sup>, which can be associated with the significant mode III tilting shown in Fig. 5(c). Frequent changes in tilting direction are confirmed at martensite/ferrite interfaces together with some martensite/ferrite interfacial crack extension where the crack front line becomes more complicated. A typical example is indicated by the arrows in Figs. 5(b) and 5(c). It can be inferred that the retarded sections of the crack front might be associated with the existence of the martensite grains.

Fig. 6(a) shows the variations in measured CTOD along the crack front line at an applied load of 60 N. The CTOD value tends to roughly increase when going from left to right. It appears to increase locally four to five times over intervals of approximately 10 to 50  $\mu\text{m}$  along the crack front line, probably because of the crack/microstructure interaction that was shown in Fig. 5. This is because the length range over which the CTOD values are locally elevated corresponds to the dimensions of the ferrite/martensite grains that are shown in Fig. 5(b). The local CTOD elevation can also be associated with the occurrence of local crack deflection shown in Fig. 6(b), providing evidence for the effects of the underlying grain dual phase structure.

Fig. 7 shows examples of crack-tip strain field shown on three different virtual cross-sections that has been calculated between applied loads of 33.6~60.0 N. It is clear that the strain distribution is far different from that obtained in typical elastic-plastic fracture mechanics. Although the measurement does not provide an exceedingly high spatial density in displacement markers, due to the relatively small number of microstructural features visible that can be utilized as strain markers, it appears most likely that the strain distribution has been affected significantly by the underlying microstructure. Fig. 7 also shows how the crack-tip strain field varies from place to place. In Fig. 7(c), vertical elongation of the crack-tip strain field is observed in both upper and lower directions. This characteristic geometry of the crack-tip strain field can be associated with the existence of considerably elongated inclusion particles in the vicinity of the crack-tip. Such particles can be clearly recognized in Fig. 5(c) as ten to twelve needle-like inclusions that align in the vertical direction.

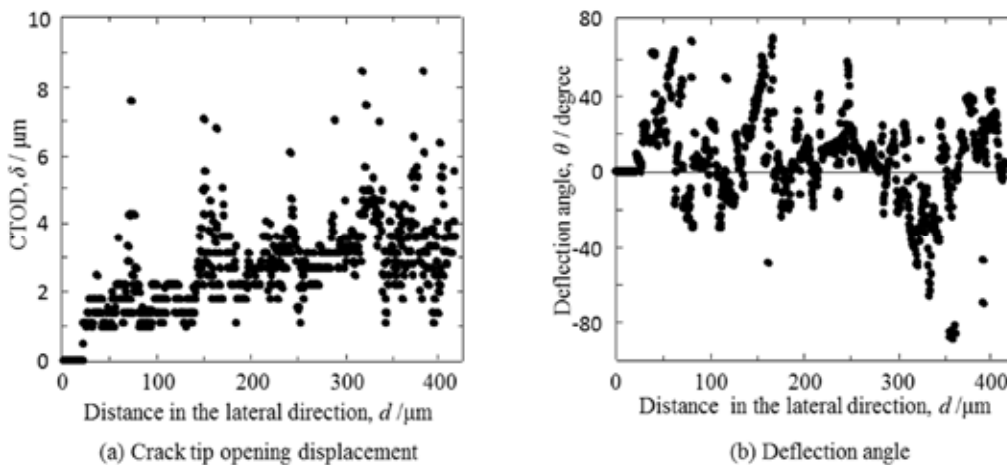


Fig. 6 Distribution of CTOD along the crack front line in (a) and corresponding deflection angle distribution in (b).

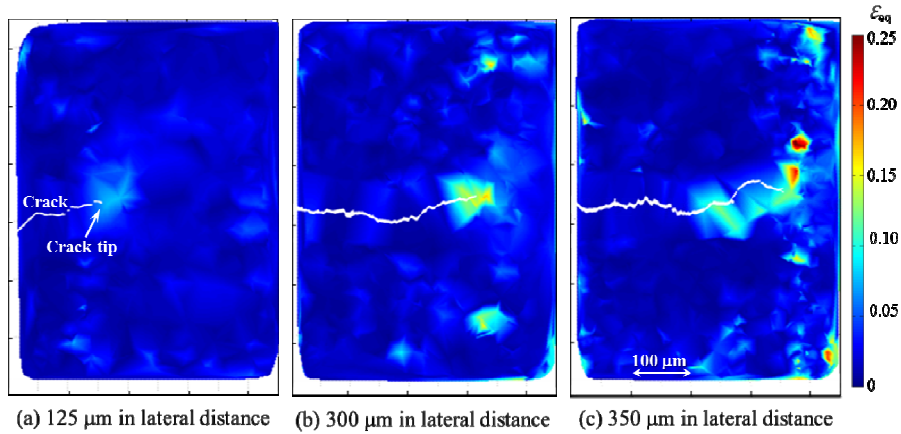


Fig. 7 The examples of crack-tip strain field shown on three different virtual cross-sections. Equivalent strain is shown in the figure.

### 3.3 Effect of creep stress on the void evolution

From the 3-D rendering of the reconstructed slices obtained from XMT on the crept samples, it is clear that the creep damage that is in-homogenously distributed in the re-constructed volume of interest was progressively increased with increase of creep stress and holding time. The series of creep tests reveal that the cavitation damage was dominated issue in the creep failure. The inset in Fig. 8 shows the method used to identify the onset of damage phase from the elongation-time curves obtained via the creep tests. The tangent intersection from the secondary and tertiary stages separates the tertiary part of creep elongation-time curve into coarsening dominated and cavitation dominated regions. Fig. 8 shows the stress dependence of the life fraction consumed in the damage phase for the steel. There seems to be a transition in the functional dependence of the ratio of time expended in damage to its corresponding creep life in the tested stress range. As the applied stress during creep decreases the ratio sharply decreases until about 155~160 MPa, after which the fall is arrested with a slight increase in the stress range 120~135 MPa. In order to explain these trends, the quantitative analysis of cavitation behavior from the 3-D rendered volumes has been carried out. The analysis results are shown in Fig. 9, in terms of variation of number density, size and volume fraction of voids with the applied creep stress. While a steady rise in the number density of voids is seen with decreasing creep stress, correspondingly a significant rise in the void volume fraction is observed only for the lowest stress. An increasing number density of voids without significant variation in its volume fraction and average void size in creep stress range 135~180 MPa implies an increase in nucleation rate of voids. At the lowest stress, however, there has been nearly a three-fold increase in volume fraction along with slight increase in the average diameter of voids and a

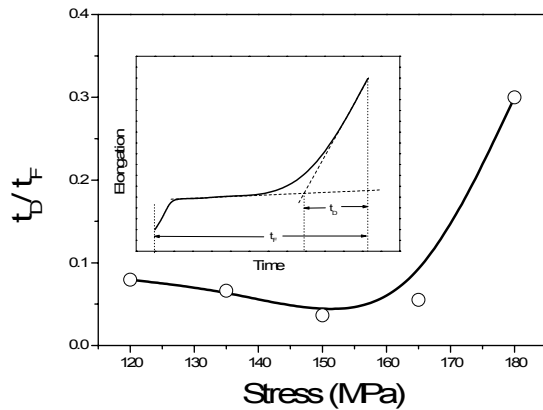


Fig. 8 A plot of the variation of the fraction of creep life expended in cavitation with stress for the 12%Cr tempered martensitic steel. The inset shows the procedure followed to delineate the period of cavitation damage from the elongation-time obtained from the creep test.

significant upswing in the number density curve, which implies the growing influence of void coalescence/growth mechanism. This is also corroborated by the presence of many of complex shaped large voids at the lowest stress. The analysis of the void size distribution shown in Fig. 9(d) also confirms the trend of increasing nucleation rate sustained even at long creep time, along with increasing influence of void coalescence. This interpretation stems from the observation that the size distribution shifts to the right only after increasing peak frequency to a defined level with increase in creep exposure times.

### 3.4 Effect of creep holding time

Creep behavior of the steel shows an extended damage period before failure above a stress of 155~160 MPa as compared with those at lower stresses. It is significant to note that at these high stresses the void nucleation rates seems to be lower as evidenced by its low number density, volume fraction and peak frequencies in void size distribution. Further from the 3-D images the spatial distribution of the voids seems to be in-homogenous. In order to understand the nature of the distribution rendering near to the areas of high number density of voids have been carried out. The rendered 3-D volume expanded near to these regions is shown for three types of creep time in Figs. 10(a), 10(b) and 10(c). It is clearly seen that with increasing creep time the appearance of aligned voids increase. The probable loci of the alignment of the voids are emphasized by the black lines in the images. It is well known that internal interfaces are the preferred locations for nucleation of creep voids in materials<sup>26)</sup>. Tempered martensitic steels contain both prior austenitic boundaries as well as packet and lath boundaries, which are known to initiate creep voids. It is thus evident from nature of the curves that the aligned voids are a part of the various boundaries present in a tempered martensitic structure. In order to investigate the association of the boundaries to these aligned voids, the specimen crept at 15216 h was

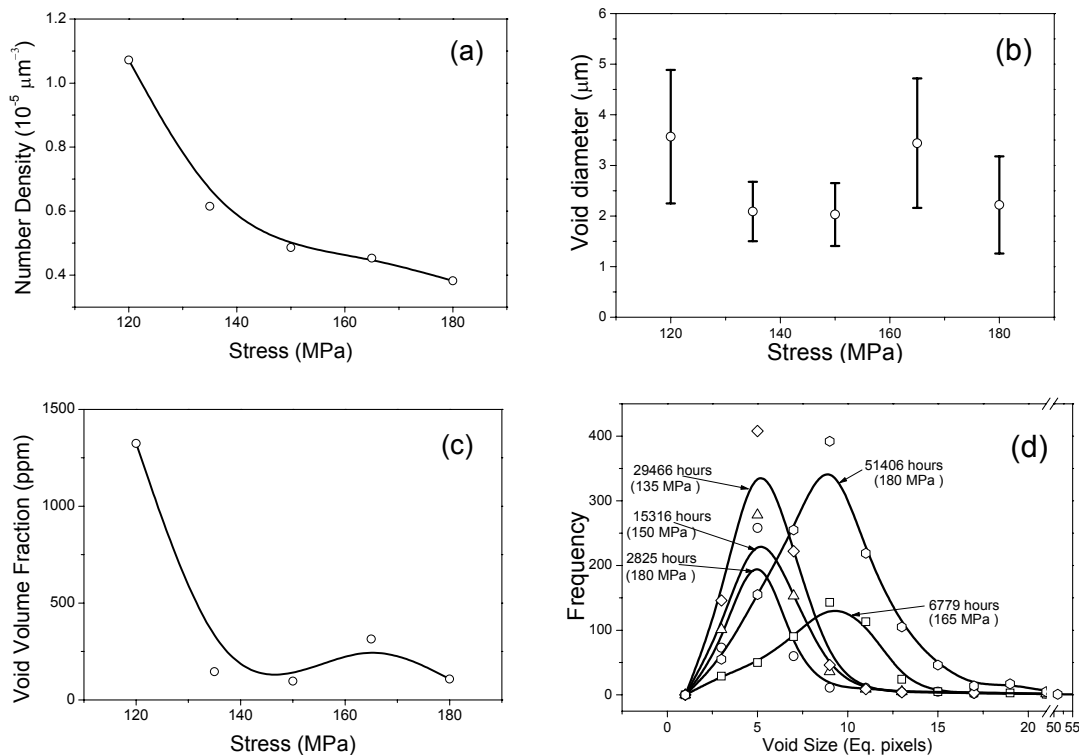


Fig. 9 Plots showing the variation of (a) number density (b) void diameter (c) void volume fraction with stress. (d) The void size distribution as a function of creep exposure time.

investigated by combined serial sectioning and OM. The twenty serial sections with a 3  $\mu\text{m}$  interval were imaged and digitized using OM. The slices were merged to create a volume dataset. One polished section of the selected sample about 9  $\mu\text{m}$  from the top was etched to delineate the prior austenitic grain boundary, which was then traced out on the corresponding digitized image of the polished slice. The volume dataset thus generated was matched with the corresponding tomography dataset on the basis of the registration of the images of voids seen in the two 3-D rendered images. Fig. 10(d) shows the result of the near matching of the 3-D rendered image. The prior austenite grain boundary located 9 $\mu\text{m}$  below the surface is seen with the voids in the tomography image. From the Fig. 10(d) it appears that void cluster marked as 'A' is associated with the prior austenite grain boundary. As it is the dominant cluster type in the volume, it may well be that in this case that voids show preference to nucleate at the prior austenite boundary as compared with packet or lath boundary located in the grain interior.

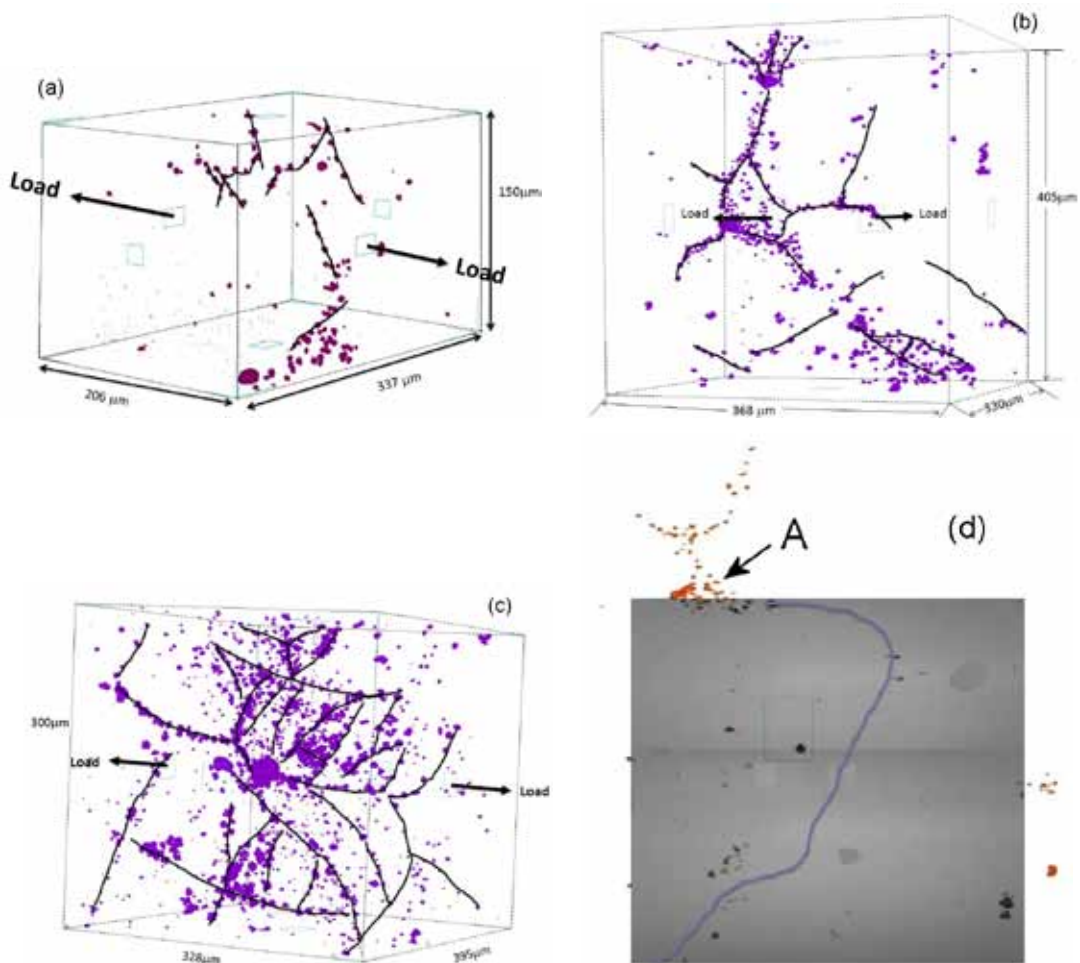


Fig. 10 An expanded 3-D rendering of the regions of high number density of voids for sample exposed to creep times of (a) 2825 h (b) 15316 h and (c) 51406 h. The black lines are the loci of the alignment of the voids. (d) The composite image of the region characterized by optical microscopy within the reconstructed, rendered and thresholded image obtained from tomography scan. The dark line within the OM characterized region is the prior austenite boundary located 9  $\mu\text{m}$  below surface. The dominant void cluster is indicated as A.

## 4. Conclusions

X-ray microtomography was employed to observe a fatigue crack in S15C steel and a void evolution by creep stress in 12%Cr alloy. A high-resolution experimental configuration enabled surprisingly superior spatial resolution of better than 1.3  $\mu\text{m}$  after optimizing experimental parameters. The spatial resolution level achieved in the present study is clearly advantageous compared to the limited past trials on ferrous materials. Owing to the high spatial resolution achieved, the details of a crack were readily observed, along with evidence of the interaction between the crack and a dual phase microstructure. After preliminary investigation of the obtained images were used to quantify crack-tip opening displacement and crack-tip strain.

From the 3D visualization of voids in the crept samples, it can be considered as one of effective methodologies to understand the in-homogenous nature of the spatial distribution of voids and its relation to the variation of the damage period with stress and time in the creep life of the steel. Due to the break-down of martensitic structure in the boundary vicinities, further precipitate coarsening can lead to acceleration of void nucleation. Therefore, there is large scale appearance of aligned voids at prior austenite boundaries that subsequently grow and coalesce. In case of the stress range 155~180 MPa, together with less cavitation inside grains, a rapid decline of the damage phase was observed as a fraction of total creep life due to the greater contribution of void growth.

It may be concluded that the use of 4D microtomography observation, combined with an advanced image analysis techniques, might offer a highly effective means of investigating various issues relating to ferrous materials. The high-resolution XMT observation achieved in the present study is of crucial importance to the development and application of such techniques.

## Acknowledgements

This work was partly undertaken as a technical research aid project of the JFE 21st Century Foundation for FY 2010. The synchrotron radiation experiment was performed with the approval of JASRI through proposal number 2010A1247.

## References

- [1] H. Toda, K. Shimizu, K. Uesugi, Y. Suzuki and M. Kobayashi: *Mater. Transactions* 51 (2010) 2045.
- [2] H. Toda, T. Hidaka, M. Kobayashi, K. Uesugi, A. Takeuchi, K. Horikawa: *Acta Mater.* 57 (2009) 2277.
- [3] R.K. Everett, K.E. Simmonds, A.B. Geltmacher: *Scripta Mater.* 44 (2001) 165.
- [4] O. Lame, D. Bellet, M.D. Michiel, D. Bouvard: *Acta Mater.* 52 (2004) 977.
- [5] K.S. Cheong, K.J. Stevens, Y. Suzuki, K. Uesugi, A. Takeuchi: *Mater. Sci. Eng. A* 513-514 (2009) 222.
- [6] T. Shobu, K. Tanaka, A. Hashimoto, J. Narita: *J. Soc. Mater. Sci., Jpn.* 58 (2009) 588.
- [7] L. Qian, H. Toda, K. Uesugi, M. Kobayashi, T. Kobayashi: *Phys. Rev. Lett.* 100 (2008) 115505.
- [8] H. Toda, S. Yamamoto, M. Kobayashi, K. Uesugi: *Acta Mater.* 56 (2008) 6027.
- [9] H. Toda, T. Nishimura, K. Uesugi, Y. Suzuki, M. Kobayashi: *Acta Mater.* 58 (2010) 2014.
- [10] S.R. Stock: *Inter. Mater. Rev.* 53 (2008) 129.
- [11] M. Kobayashi, H. Toda, Y. Kawai, T. Ohgaki, K. Uesugi, D.S. Wilkinson, T. Kobayashi, Y. Aoki, M. Nakazawa: *Acta Mater.* 56 (2008) 2167.
- [12] Q. Zhang, H. Toda, Y. Takami, Y. Suzuki, K. Uesugi, M. Kobayashi: *Philos. Mag. A* 90 (2010) 1853.
- [13] H. Toda, S. Masuda, R. Batres, M. Kobayashi, S. Aoyama, M. Onodera, R. Furusawa, K.

- Uesugi, A. Takeuchi, Y. Suzuki: *Acta Mater.* 59 (2011) 4990.
- [14] H. Toda, E. Maire, S. Yamauchi, S. Tsuruta, T. Hiramatsu, M. Kobayashi: *Acta Mater.* 59 (2011) 1995.
- [15] J.Y. Buffiere, E. Maire, P. Cloetens, G. Lormand, R. Fougères: *Acta Mater.* 47 (1999) 1613.
- [16] W. Ludwig, J.Y. Buffière, S. Savelli, P. Cloetens: *Acta Mater.* 51 (2003) 585.
- [17] A. Tekeuchi, K. Uesugi, H. Takano, Y. Suzuki: *Rev. Sci. Instru.* 73 (2002) 4246.
- [18] G.T. Herman: *Image reconstruction from projections*, Academic Press, San Francisco, (1980) 1.
- [19] W.E. Lorensen, H.E. Cline: *Comput. Graph. (ACM)* 21 (1987) 163.
- [20] H. Toda, E. Maire, Y. Aoki, M. Kobayashi: *J. Strain Anal. Eng. Des.* 46 (2011) 1.
- [21] C.B. Barber, D.P. Dobkin, H. T. Huhdanpaa: *ACM Trans. Math. Soft.* 22 (1996) 469.
- [22] J.A. Seibert, J.M. Boone: *J. of Nuc. Med. Tech.* 33 (2005) 3.
- [23] H. Toda, I. Sinclair, J.Y. Buffiere, E. Maire, T. Connolley, M. Joyce: *Phil Mag A.* 83 (2003) 2429.
- [24] H. Toda, I. Sinclair, J.Y. Buffiere, E. Maire, K.H. Khor, P. Gregson: *Acta Mater.* 52 (2004) 1305.
- [25] Y. Motoyashiki, A. Bruckner-Foit, A. Sugeta: *Fatigue Fract. Eng. Mater. Struct.* 30 (2007) 556.
- [26] M.E. Kassner, T.A. Hayes: *Int. J. Plasticity* 19 (2003) 1715.